Department of Physics and Astronomy
University of Heidelberg

Bachelor Thesis in Physics
submitted by

Niccolò Rigi-Luperti

born in Tübingen (Germany)

2020

Investigation and improvement of metastable Argon densities in a helical resonator driven plasma for the ArTTA experiment

This Bachelor Thesis has been carried out by
Niccolò Rigi-Luperti
at the
Kirchhoff-Institut für Physik in Heidelberg
under the supervision of
Prof. Dr. Markus K. Oberthaler

Abstract

In this thesis, a low-pressure inductively driven argon plasma was investigated, a setup used to generate metastable argon atoms for the ArTTA experiment. Firstly, broadening effects were studied with a Doppler free absorption setup. It was found that pressure broadening has much less impact than originally expected and the Lamb-Dip width most likely is dominated by power broadening.
This measurement setup was also employed to determine line-integrated metastable densities in the plasma. This is interesting since high metastable density improves the performance of the ArTTA machine. The analysis was done by changing both geometry and operation of the helical resonator, the device which generated the plasma. It was found that already small changes in the resonators configuration changed metastable densities significantly, and the best explored configuration improved metastable densities by a factor of 4 compared to the worst.

Zusammenfassung

In dieser Arbeit wurde ein induktiv getriebenes Argonplasma bei niedrigen Drücken untersucht, welches im ArTTA Experiment benutzt wird um metastabile Argonatome zu erzeugen. Als Erstes wurde Linienverbreiterung durch eine Dopplerfreie Sättigungsspektroskopie untersucht. Es stellte sich heraus, dass Druckverbreiterung eine sehr viel kleinere Auswirkung hatte als ursprünglich angenommen und dass die Lamb-Dip Breite sehr wahrscheinlich dominiert wird von Sättigungsverbreiterung.
Derselbe experimentelle Aufbau wurde auch benutzt um linienintegrierte Dichten des metastabilen Zustandes im Plasma zu messen. Das ist interessant da hohe Metastabilendichten die Effizienz der ArTTA Maschine verbessern. Zur Untersuchung wurden sowohl die Geometrie als auch die Betriebsart des Helical Resonators, dem Gerät das das Plasma generiert, verändert. Es stellte sich heraus, dass bereits kleine Änderungen in der Konfiguration des Resonators die Metastabilendichte signifikant beeinflussten. Die beste gefundene Konfiguration führte zu einer Verbesserung in der Metastabilendichten um einen Faktor von 4 verglichen mit der schlechtesten Konfiguration.

Contents

1 Introduction

The dating of water and ice samples is of big interest in environmental sciences. It gives important information on the transport and mixing behaviour of groundwater, continental water, oceans and glaciers. These water systems are of high scientific, but also social and political interest and are modelled and monitored intensively. To this end, accurate dating techniques are needed.

In the case of water and ice samples, the radioactive argon isotope ^{39}Ar can be used for dating. It has a lifetime of 269 years, which allows a dating range of 50-1000 years, which is a time range not reached by any other tracer. Argon is also chemically inert, another helpful property. However, due to its extremely low abundance of $8.23 \cdot 10^{-16}$, ^{39}Ar could only be measured by Low-Level Counting in an underground laboratory at the university of Bern. It was initialized in 1976 and has been running since [1].
In 1994, the Argonne National Laboratories near Chicago (name similarity with argon purely coincidental) reported dating measurements on ^{39}Ar, through an adapted Accelerator Mass Spectrometry at their accelerator facility [2]. However, these measurements were not continued, probably because the heavily scheduled accelerator was too costly, so no routine measurements on argon were done.
Then in 1999, Atom Trap Trace Analyses (ATTA) was developed, a new all-optical dating technique in which specific isotopes could be addressed individually via laser cooling and trapping, which allowed comparatively small table-top setups, and reduced sample sizes to litres instead of tonnes and measurement time to days instead of weeks [3]. It was however built for krypton isotopes and not for argon at that time.
Lastly, in Heidelberg in 2008 experimental work was initiated to adapt the ATTA laser dating technique to argon [4]. The experiment and the research group was consequently named ArTTA. The new setup required multiple improvements in detection efficiency compared to the case with krypton, because ^{39}Ar has an abundance of 10^{-4} compared to the krypton isotopes, making it four orders of magnitude more difficult to detect. The first measurements with ^{39}Ar were achieved in 2014 on groundwater dating, in which 3.8 atoms were counted per hour [5]. Since then, this detection efficiency was improved by two orders of magnitude [6] [7], and optimization of the ArTTA experiment is ongoing research.

In this thesis, we investigate one part of the ArTTA setup in more detail, namely, the helical resonator and it's argon plasma. This is a stage at the beginning state of the experiment, were atoms are excited to higher states, from where on they can then be cooled and trapped by conventional lasers.

2 Theory

This chapter gives an overview over the underlying concepts used in this thesis.

2.1 Argon level structure

In the ArTTA experiment, an atomic electronic dipole transition needs to be driven for laser cooling and detection. In an ideal case, this transition would be performed from the ground state, $1s_1(J = 0)$, Paschen Notation. However, the closest available transitions are of wavelengths 105nm and 107nm, to the states $1s_1(J = 1)$ and $1s_4(J = 1)$. This is shown in the argon level structure in figure 1. These short wavelengths arise because argon is a noble gas and has a closed shell. For such short wavelengths currently no laser systems are available. Optics would also pose a problem in this UV regime, as they degrade on the order of days [8]. This leads to the usage of metastable states.

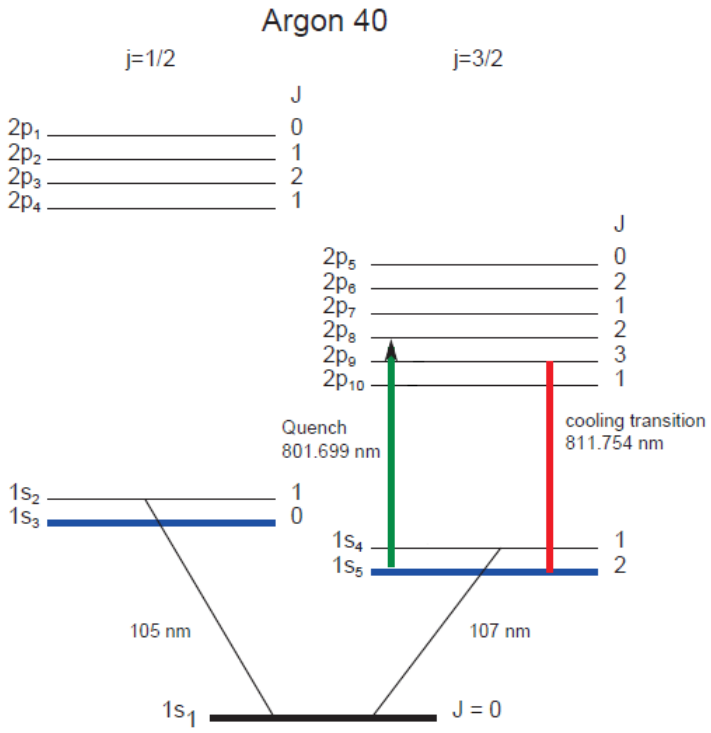

Figure 1: Level structure of argon 40, for the lowest 15 levels [4].

Metastable states are states that have dipole-forbidden decay channels, which gives them long lifetimes. In argon, the state $1s_5(J = 2)$ is such a metastable state, with a lifetime of 35 seconds. This is because of its angular momentum difference $\Delta J = 2$ to the ground state, allowing only quadrupole relaxation which occurs at a much smaller probability. From the metastable state $1s_5$, optical dipole transitions at ranges 700-800nm are available, making current diode laser systems applicable. Specifically for the ArTTA experiment, the transition $1s_5(J = 2)$ to $2p_9(J = 3)$ ($\lambda_0 = 811.754$nm) is chosen as the cooling transition, because the $J = 3$ forces a decay back into $J = 2$ making it a closed transition. Another available transition $1s_5(J = 2)$ to $2p_8(J = 2)$ ($\lambda_0 = 801.699$nm) is used as a quench transition, allowing to deplete the metastable state.

The considerations above apply for both the isotopes ^{40}Ar and ^{39}Ar. While the latter one is eventually used for dating, the former is much more abundant making it a practical tool for testing new ideas. As both have similar behaviour, the gained knowledge can then be transferred. In this thesis all measurements were done on ^{40}Ar.

To excite the atoms into in the metastable state without the use of lasers, a plasma is generated.

2.2 Plasma

A plasma can be created by applying a strong oscillating external electric field. This field accelerates electrons and ions, which then collide in our case with argon atoms and excite them in any higher state, or ionize them. While the argon atoms are excited to any states, a fraction of them (ca. 10^{-4} in the current source setup) ends up in the desired metastable state $1s_5$, from where they can be accessed with laser light for the rest of the experiment.

Figure 2: Plasma burning in the experiment.

The main production mechanism for $1s_5$ is direct excitation via high energy electron collision from the ground state [9].

$$Ar(1s_1) + e(\geqslant 11.55eV) \longrightarrow Ar(1s_5) + e \quad \text{(el. excitation)} \tag{2.1}$$

In low-pressure plasma, as in our case, a major loss mechanism for $1s_5$ is low energy electron collision, quenching to the nearby $1s_4$, $1s_2$ states, which then relax via dipole transitions quickly to the ground state.

$$Ar(1s_5) + e \longrightarrow Ar(1s_4; 1s_2) + e \quad \text{(el. quenching)} \tag{2.2}$$

$$Ar(1s_4; 1s_2) \longrightarrow Ar(1s_1) + h\nu \quad \text{(relaxation)} \tag{2.3}$$

Other loss mechanisms of Ar($1s_5$) are for example ionization, two-body collision and de-excitation at the wall. Modelling all these interactions is its own research area, thus in this work the metastable densities are only investigated experimentally.

Additional interactions can be achieved if multiple gas species are mixed together. The introduction of a second species gives rise to new interactions that might be beneficial for the plasma at use. In the case of argon metastables, experiments have been performed e.g. with He [10], Kr, Xe, N_2, He [11], Cl_2, BCl_3 [12], and O_2,CF_4 [13]. In most cases a reduced metastable density was reported, but in some, most noticeable [10], an increased metastable density was reported.

2.3 Line-broadening effects

The most fundamental broadening effect of an atomic transition is its natural line width, with the well known Lorentzian shape. In a plasma, additional line broadening effects happen due to the motion and interaction of the atoms with each other. We will focus on two broadening effects that will be studied in more detail: Doppler broadening and pressure broadening.

2.3.1 Doppler broadening

Doppler broadening arises due to the Doppler shift. Applied to atoms and lasers, it means that if an atom moves with velocity $\vec{v}$ relative to a laser beam with wave vector $\vec{k}$, it experiences the frequency of the laser shifted by an amount $\Delta\nu = \vec{v} \cdot \vec{k}/2\pi$. In the special case in which atom and laser beam move parallel (-) or antiparallel (+) to each other, the frequency shift is simplified to $\Delta\nu = \pm(v/c)\nu_0$, where ν_0 is the original laser frequency and c the speed of light. In case of a thermal atom ensemble, the atoms velocity is given by the Maxwell-Boltzmann velocity distribution which has Gaussian shape. As the Doppler shift is linearly linked to velocity, the absorption line shape $g(\nu)$ is Gaussian as well [14]:

$$g(\nu) = \left(\frac{4\,ln(2)}{\pi \cdot {\Delta\nu_d}^2}\right)^{1/2} exp\left[-4\,ln(2)\left(\frac{\nu-\nu_0}{\Delta\nu_d}\right)^2\right] \tag{2.4}$$

with the FWHM Doppler width

$$\Delta\nu_d = \sqrt{\frac{k_B T \cdot 8\,ln(2)}{mc^2}} \cdot \nu_0 \tag{2.5}$$

where ν_0 is the resonant transition frequency, k_B the Boltzmann constant, T the gas temperature and m the atom mass. Due to temperature being the only free parameter, the Doppler width $\Delta\nu_d$ is a common tool for measuring plasma temperatures.

2.3.2 Pressure broadening

This section is mainly based on [15], in which pressure broadening is discussed concisely. In a plasma, the major source of pressure broadening comes from the interaction of the radiating atom with surrounding particles, which cause a frequency disturbance and a phase shift onto the radiation. The phase shift is given by $\Delta\phi = C_k/r^k$, where r is the distance to the perturber, and k tells the type of interaction. Direct collisions do also occur, but the field interactions are more dominant. The most important of them are: Linear Stark effect: k=2, Resonance interaction between identical particles: k=3, Quadratic Stark effect: k=4, and Van-der-Waals (VdW) interaction: k=6. Each of them is shortly discussed in the following. All pressure broadening effects have in common that their line shape is a Lorentzian [16].

Linear and Quadratic Stark broadening occurs when an emitting atom is perturbed by the electric field of an ion or electron at distance r. The linear Stark effect exists only for hydrogen-like atoms. The interaction is quadratic ($1/r^4$) for all other atoms. This is because the linear Stark effect occurs only in systems where there is a degeneracy or near-degeneracy between levels that are connected by a dipole transition [16]. Higher order Stark effects are reported to be usually very small compared to the linear one [16]. Formulas found for the Stark broadening were quite evolved containing parameters not known in this work. As a result, we haven't estimated the quadratic Stark effect.

Resonance broadening is the interaction between identical atoms and has the form of a dipole-dipole interaction. The wave functions of the ground and the excited states combine to form a non-zero dipole moment. The interaction is proportional to $1/r^3$ and the oscillator strength f_{21}. The lines are symmetrically broadened and unshifted. The resonance broadening width can be approximated by [15]

$$\Delta\lambda = \frac{3}{16}\left(\frac{g_1}{g_2}\right)^{1/2} n\frac{\lambda_0^3 e^2 f_{21}}{\pi^2 \epsilon_0 m_e c^2} \tag{2.6}$$

with the oscillator strength

$$f_{21} = \frac{m_e \epsilon_0 c^3}{2e^2 {\nu_0}^2} A_{21} \tag{2.7}$$

where g_1 and g_2 are statistical weights of the lower and upper states, e and m_e the charge and mass of the electron, ϵ_0 the vacuum permittivity, λ_0 and ν_0 the transition wavelength and frequency, c the speed of light, n the atom number density, and f_{21} the dimensionless transition oscillator strength, which is given in eq. 2.7 in terms of the Einstein coefficient. The respective broadening in frequency space is given by $\Delta\nu = c/\lambda_0 - c/(\lambda_0 + \Delta\lambda)$, which can be approximated by $\Delta\nu = c\Delta\lambda/\lambda_0^2$ to an excellent degree.

Van-der-Waals broadening describes the dipole-dipole interaction between the radiating atom and surrounding neutral atoms. One approximation to the FWHM of Vander-Waals broadening is given in [10] as:

$$\Delta\nu = \sum_i \left(\frac{2\gamma_0}{N}\right)_i \left(\frac{T}{T_{0i}}\right)^{0.3} \left(\frac{p_i}{k_B T}\right) \tag{2.8}$$

where the sum is taken over the neutral gas species with partial pressures p_i that are colliding with the absorber atom. The parameters $(2\gamma_0/N)_i$ are collisional broadening parameters measured at a reference temperature T_{0i}. In [17] measurements are reported as $(2\gamma_0/N)_i = 1.8 \cdot 10^{-16}$Hz m^3, which refer to argon-argon collisions at T_0=300 K for the $1s_5$-$2p_9$ cooling line, and similarly $2.3 \cdot 10^{-16}$Hz m^3 for the $1s_5$-$2p_6$ line.

The ideal gas law $n = p/(k_B T)$ was assumed for this low pressure regime, as can for example be seen in equation 2.8.

2.3.3 Estimations

To conclude, a sample calculation is conducted to compare the predictions of natural, Doppler, resonance and VdW broadening. The quench transition $1s_5$-$2p_8$ at pressure $3 \cdot 10^{-2}$mbar and temperature 300K is chosen for this comparison, as it is the transition that

is later investigated in the experiment. The statistical weights are $g_{1s5} = 5$ and $g_{2p8} = 5$, listed e.g. in [18]. For $(2\gamma_0/N)_i$, an average of the two given values is taken. The resulting line widths are listed in table 1.

Table 1: Theoretical predictions for different line broadening mechanisms, calculated for $3 \cdot 10^{-2}$mbar, 300K, transition $1s_5 - 2p_8$.

Broadening mechanism	**Line width $\Delta\nu$**
Natural lifetime	9.28 MHz
Doppler broad.	730 MHz
Resonance broad.	23 MHz
V.d.Waals broad.	0.1 MHz

Let us briefly discuss the results in table 1. The most striking observation is that in the case of low pressures, Doppler broadening dominates over all other effects by one to two orders of magnitude. The calculated value of 730 MHz for Doppler broadening is a lower bound, because the temperature in the plasma might be higher than room temperature, but surely not lower. Resonance broadening and natural line broadening are on the same order of magnitude, with resonance broadening being larger by a factor of about 2. Vander-Waals broadening can be neglected in this case, it is two orders smaller than the natural line width. Experimentally this leads to the prediction that the absorption shape will be to a good approximation Gaussian due to Doppler broadening, and if Doppler broadening is subtracted (see next section), the remaining width would be about twice the natural line width.

To produce pressure and Doppler broadening on the same order of magnitude, the pressure would need to be about 30 times higher than the pressure chosen in table 1, which was a typical pressure from the experiments conducted in this thesis. Then, the resulting line shape would be described by a convolution of both broadening effects, known as a Voigt Profile. In the case of a dominating Doppler effect, the Voigt profile can be approximated by a Gaussian.

2.4 Doppler free absorption spectroscopy

Doppler free absorption spectroscopy is a technique that allows to overcome the Doppler broadening effect. Two laser beams with the same frequency are sent through a plasma (or gas in general), overlapping spatially, but with opposite propagation directions. The beams are operated in pump and probe mode, where one beam is more intense than the other (pump) but only the weaker one (probe) gets measured after passing the plasma. If both beams have the frequency ν which is near an atomic transition frequency ν_0, two cases can be distinguished:
$\nu \neq \nu_0$: The two beams get absorbed by different atoms with velocities $\pm v$, where the velocity v is such that the Doppler shift cancels the lasers detuning leading to resonance. As the beams propagate in opposite directions, they address different velocity classes of atoms. Thus the lasers are absorbed independently from each other and burn two separate holes into the absorption spectrum, symmetrically spaced around the center of the Doppler profile.
$\nu = \nu_0$: The two beams get both absorbed from atoms with velocity $v = 0$, as the lasers are already on resonance. This means that both lasers now address the same atoms. The

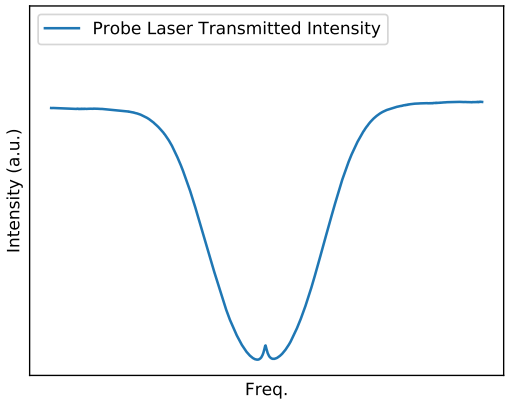

Figure 3: Lamp-Dip at the bottom of the Doppler valley. The shown spectrum is from a measurement.

pump beam depletes the lower level allowing the probe beam to pass with less absorption. Additionally the probe beam can trigger stimulated emission increasing further its intensity and leads to a small intensity peak near the transition frequency. This peak is called Lamb-Dip and can be seen in figure 3, where a typical measurement is shown.
If a Lamb-Dip is seen, the Gaussian profile can be subtracted from the measurement, effectively removing the Doppler broadening from the measurement. On the remaining Lamp-Dip, the other broadening effects can then be studied, and it can also be used for laser locking. Without a Doppler free absorptoin spectroscopy these further detections would not be possible.

2.5 Metastable density calculation

For an estimation of the $1s_5$ metastable density inside the plasma, the Lambert-Beer Law is used. Its general form reads

$$nL\sigma = ln(I_0/I) \tag{2.9}$$

where n is the density of the absorbing species, L the effective absorption length, σ the absorption cross section, I_0 the incident and I the transmitted intensity. Some considerations are needed to connect this general law to the measurements employed in this thesis.

First, the laser has to be tuned onto an atomic resonance transition from the metastable state to an upper state. Assuming a much more populated lower level than upper level, stimulated emission can be neglected, and only absorption (and spontaneous emission) takes place. The absorption signal is then directly linked to the density of the lower level, allowing to probe its density. For a chosen transition, the averaged absorption cross section is [19]

$$\overline{\sigma_{21}} = \frac{\lambda_0^2}{4}\frac{A_{21}}{2\pi\Delta\nu} \tag{2.10}$$

where λ_0 is the wavelength of the transition, A_{21} the Einstein coefficient for spontaneous emission from the upper level, and $\Delta\nu$ the FWHM of the absorption profile. In cases such as the one encountered in this experimental setup, the absorption profile width is mainly given by the Doppler width $\Delta\nu_d$. Secondly, the line broadening of the plasma has to be taken into account. This can be done by integrating over a small frequency range around the center transition ν_0, where absorption takes place [20]. In equation 2.11, we write this small scanning range around a center frequency as $[range\ \nu_0]$. Thirdly, the plasma is spatially non-uniform, a laser going through only resolves an averaged

density $\langle n_{1s5} \rangle$. At last, the effective absorption length L might be difficult to measure independently, because of the non-uniform plasma. This can be addressed by defining the measurement to be the line-integrated density $\langle n_{1s5} \rangle L$, where no knowledge of L is needed. After these considerations are implemented in the Beer-Lambert law 2.9, one can divide by the cross section. This then gives the line-integrated metastable density expressed through measured absorption intensities and constants:

$$\langle n_{1s5} \rangle L = \frac{4}{\lambda_0^2} \frac{2\pi\Delta\nu}{A_{21}} \int_{[range\, \nu_0]} ln\left(\frac{I_0(\nu)}{I(\nu)}\right) d\nu \tag{2.11}$$

where $I_0(\nu)$ is the incident intensity on the plasma and $I(\nu)$ the transmitted intensity after the plasma, and $\Delta\nu$ the measured FWHM of the absorption profile.

For the purpose of this work, the constants are mostly unimportant, as we are only interested in relative changes. Thus for all figures only the non-constant part is calculated and plotted. Still for completeness, the explicit values for the employed quench transition $1s_5$ to $2p_8$ are $A_{21} = 9.28 \cdot 10^6$Hz and $\lambda_0 = 801.699$nm.

2.6 The helical resonator

Helical resonators are devices from signal processing, where they are used as narrowband filters. They have high Q-Factors, which means they have sharp resonance peaks, and the peak energy stored inside the resonator per oscillation is high compared to the energy lost per cycle. This property of high energy storage makes them beneficial for plasma generation.

A helical resonator consists of a helically turned coil (the antenna) and a surrounding conductive shield. One end of the antenna is connected to the shield, the other end is left open. Figure 4 shows a sketch and a picture.

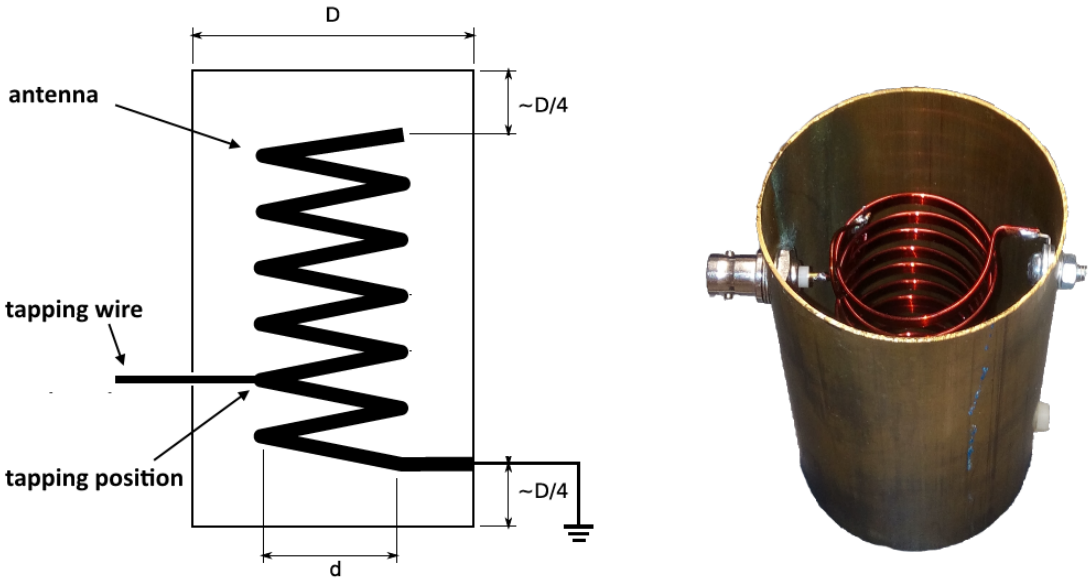

Figure 4: Sketch and picture of a helical resonator. Taken from [21].

When an oscillating signal enters into the antenna, wavelengths that are multiple quarters of the antennas length are enhanced and create standing waves, while all other wavelengths are suppressed. The condition is written as $(\lambda/4)n = l$, where l is the length of the antenna and n any integer. For n=1 the resonator is operated in the quarter-wave mode, where one quarter of the wavelength fits into the antenna which is the mode used in this work. If an RF signal is transmitted onto the antenna at resonance frequency, an oscillating electric field builds up inside the resonator, which can then be used to drive a plasma. The plasma is thus driven inductively. Compared to a cathode-anode setup, this has the advantage of reduced sputtering, especially metallic sputtering, which could degrade the plasma source.
The resonance frequency f_0 of an unloaded resonator and its quality factor Q can be computed with the following empirical formulas [22],

$$f_0 = \frac{1900}{ND} \tag{2.12}$$

and

$$Q = 50 D {f_0}^{1/2} \tag{2.13}$$

where N is the number of turns of the antenna and D the diameter of the shielding, given in units of inches. In these formulas, f_0 is given in units of MHz, and Q is dimensionless.

2.6.1 Tapping wire

A further component of the resonator is a small tapping wire. It connects the BNC-Plug on the resonator to the antenna. Incoming signals trough the BNC-Plug are then forced to first pass the antenna before they reach the grounded shield. The wire can be seen on the left in figure 4. The position where the tapping wire is soldered onto the antenna should be chosen carefully, as it changes the impedance of the resonator. To minimize reflections, the impedance of the resonator should be the same as the impedance of the BNC-cable. This detail is discussed in the following section.

2.6.2 Impedance matching

Impedance matching is a technique from electronics, which is used for the operation of the helical resonator. It concerns the situation where one wants to transmit an oscillating signal from a source into a load, via a transmission line.

Maximum power transfer For describing power transfer from source to load, two observables are needed. Firstly, the power P_{Ld} delivered into the load. Second, the efficiency η of the system. This is the ratio of power lost in the source as dissipated heat versus the power delivered into the load. Both P_{Ld} and η depend on the resistances of source and load. The equations are given below, and a graph is given in figure 5. To deliver maximum power into the load, the resistances should match, $R_{Ld} = R_{Src}$. To have maximum efficiency on the other hand, the load resistance should be much bigger than the source resistance, $R_{Ld} >> R_{Src}$. It is assumed that a constant voltage V is applied at the source.

$$P_{Ld} = I^2 R_{Ld} = \left(\frac{V}{R_{Ld} + R_{Src}} \right)^2 R_{Ld} \tag{2.14}$$

$$\eta = \frac{R_{Ld}}{R_{Ld} + R_{Src}} \tag{2.15}$$

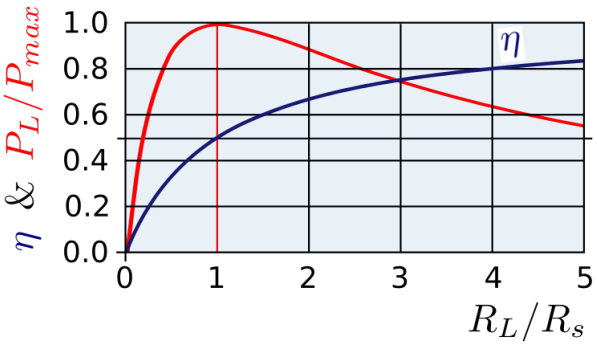

Figure 5: Power transfer from source to load. Figure taken from public domain.

When the load receives the most power, the same amount of power is also dissipated as heat in the source. As R_{Ld}/R_{Src} increases, one can no longer deliver the maximal power into the load, but, the efficiency of the total system increases, that is, the percentage of power delivered into the load relative to the total power delivered to the total system increases. If one does not care about lost heat, equal resistances are the best choice, and more generally, the condition $Z_{Ld} = Z^*_{Src}$ applies for complex impedances. The source can then provide the most power to the load, at the cost that the source then also dissipates the same amount of power as heat.

Minimal reflection Reflections are an additional effect that can occur at the end of the transmission line, where it connects to the load. There, the signal can be reflected from the load back into the source. This can damage some sources. Reflections are minimized if the impedance of the load is equal to the impedance of the transmission line: $Z_{Ld} = Z_{Line}$. Reflections can only occur if the transmission line length is at least on the order of magnitude of the transmitted wavelengths. For lines much shorter than that, no reflections occur, even at an impedance mismatch.
In a system with limited impedances, a choice needs to be made between power transfer, efficiency and reflections.

3 Experimental setup

In this chapter, the single components of the experimental setup are introduced.

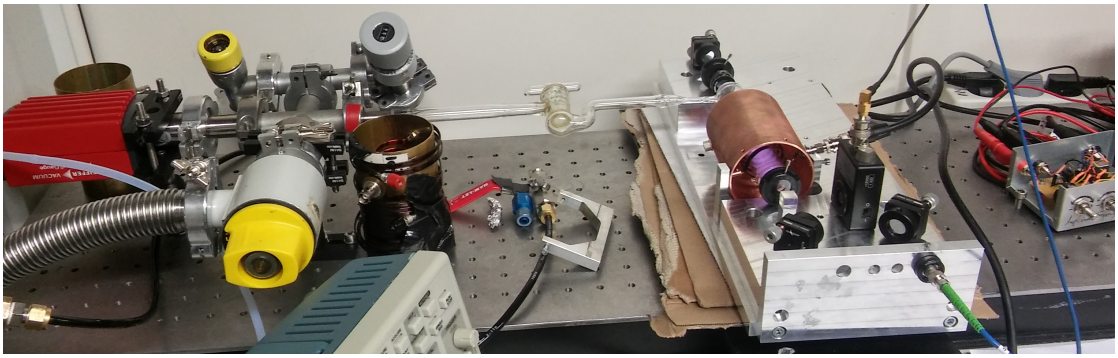

Figure 6: Vacuum gas mixing and plasma spectroscopy setup.

3.1 Resonators

Two helical resonators were used in this work. One with N=12 windings and antenna length $l = 126$cm, shown in fig. 4, and a second one with N=5 windings and antenna length $l = 53cm$, shown in figures 16 and 17. Both had a shielding with diameter D = 65mm. The first resonator design is used in spectroscopy cells for laser locking, the second is designed to produce metastable atoms for the ArTTA experiment. The resonance frequencies of both resonators are given in table 2. The theoretical values were calculated with eq. 2.12, the measurements were done with a Vector Network Analyser (VNA) and within the plasma setup.

Table 2: Resonance frequencies of the two employed Helical Resonators.

	f_0 (theoretical)	f_0 (VNC measurement)	f_0 (Plasma measurement)
Res. N = 12	62 MHz	65±2 MHz	64±5 MHz
Res. N = 5	148 MHz	146±2 MHz	145±5 MHz

The resonators were driven with an RF signal from a 1W amplifier. The amplifier received the signal from a VCO (voltage controlled oscillator), in which the RF signal was generated. With the VCO, the frequency could then be tuned by hand. An Impedance Matching Box was available, that could be inserted between Amplifier and Resonator, through two 1m long BNC-Cables coming out of the matching box. It allowed to optimize power transfer and minimize reflections, as described in detail in section 2.6.2.

3.2 VCO

VCOs are electronic devices that generate an electric oscillating signal whose frequency can be tuned via an input voltage. In the lab, the VCO-Box is fed with a constant voltage, and by means of an two additional potentiometers the frequency and amplitude of the generated signal can be tuned by hand. The amplitude was set to maximum for all measurements. In this work two VCOs with frequency ranges 50-100 and 130-220 MHz were used (Minicircuit POS-100 and POS-300).

3.3 Vacuum setup

A vacuum setup was used to direct a certain amount of argon gas, helium gas and air into a glass cell, in which plasma could be ignited. The setup is shown in figure 7. Argon and helium bottles were connected via dosing valves to the vacuum section. The helium bottle could also be omitted, in which case the dosing valve could be used to let room air in the vacuum section. The vacuum was constantly pumped by a membrane pump and a turbo molecular pump (Pfeifer HiCube 80) and pressure was monitored with a gauge. The glass cell was 15cm long and 2cm in diameter, which allowed to place the helical resonator around it.

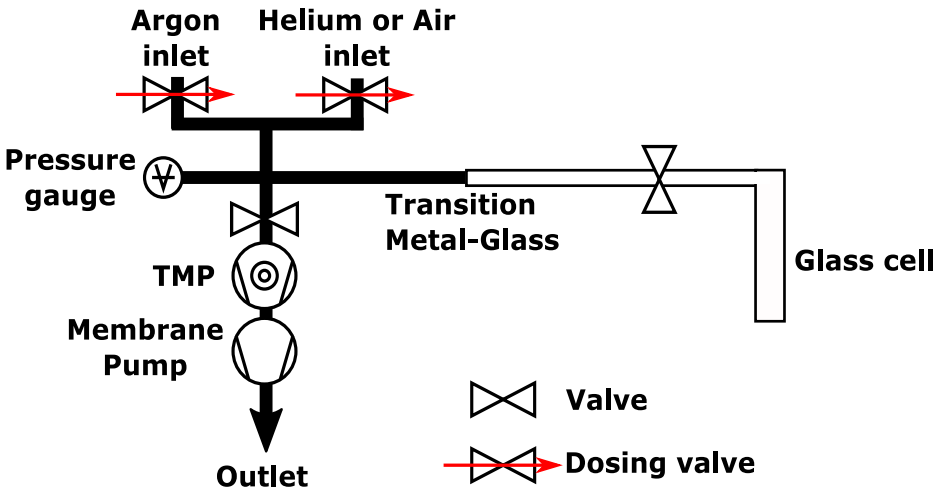

Figure 7: Schematic of the vacuum setup.

Through flow
The vacuum system was always operated in the through flow mode. That means, the argon bottle was constantly open and gas was constantly pumped from the bottle trough the system to the outlet (and the same for helium and air, when applied). Through adjusting the dosing valves at the two inlets, a desired pressure inside the glass cell could be set.
The pressure in the cell was varied between $8 \cdot 10^{-3}$mbar and $2 \cdot 10^{-1}$mbar. For lower pressures the plasma just vanished and could not be reignited. For higher pressures, the pumping system reached its limit capacity.

3.4 Laser setup

A diode laser was used (Toptica DLpro), tuned onto the quench transition $1s_5$-$2p_8$. The laser frequency could be scanned through a small frequency range via a piezo-electric element. The absorption free spectroscopy described in section 2.4 was realized in a simplified form, where a single laser beam was used for both pump and probe. The beam was linearly polarized, sent through the plasma and was reflected with a mirror back into the plasma. A $\lambda/4$ wave-plate and a polarization beam-splitting cube (PBC) were used to deflect the returning beam after the plasma into a diode. Mirrors were adjusted until incoming and reflected beam overlapped and a Lamb-Dip could be observed in the absorption spectrum. The mirrors, $\lambda/4$ plates, PBC and measuring diode were mounted fix onto a solid aluminium block, to which laser light could be connected via a fiber. The setup is shown in figure 8.

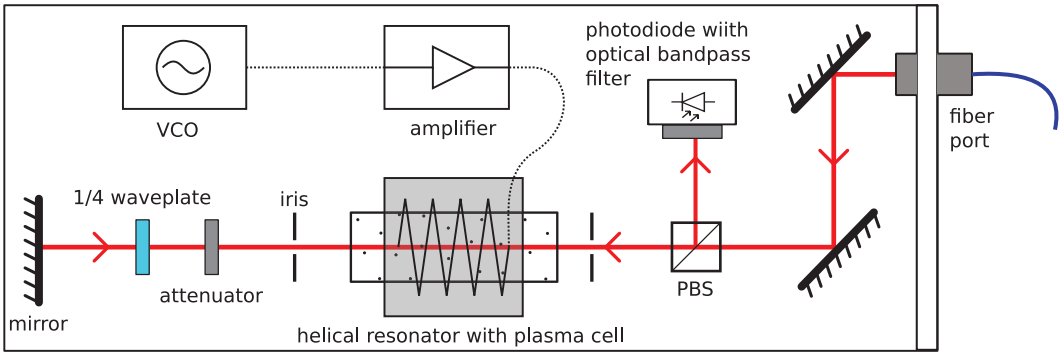

Figure 8: Schematic view of the spectroscopy setup. Figure taken from [21].

Alignment to glass cell

The spectroscopy block could be moved in and out of the cell setup. This had to be done every time the resonator was changed. Careful realignment of the block was necessary, because small changes in laser angle against the glass cell (few degrees) already changed significantly how much light was transmitted through the cell. It was chosen to align the block such that the transmitted laser light trough the empty glass cell was $1.8 \pm 0.1V$ on the diode. This value was chosen since different alignments fluctuated around it, making it the value that could be reproduced most consistently.

3.5 Smartphone spectroscopy

When the vacuum was first set up, no Doppler valley could be observed, even though plasma was visibly burning. A Doppler valley immediately appeared when a second cell (an old closed one, from the lab) was inserted into the same laser. This led to the assumption that the plasma in the new cell might be contaminated with impurities, that are other elements than argon.
To investigate the plasma, a smartphone spectrometer was built, following DIY online instructions in [23]. This spectrometer could be built in one afternoon. It consisted of cardboard and DVD piece that was cut out, both mounted onto the smartphone of the author, the full setup is shown in figure 9. The cardboard was used to form a box with a small entrance slid in the front. From the DVD-R, a transparent layer was ripped off and glued inside the box at an angle to the entrance slit. The layer from the DVD was its data line, which for a 4.7GB storage capacity is manufactured with an grating of 1350 Lines/mm, which is also the reason why CDs and DVDs appear so rainbowy. Holding the entrance of the cardboard slit against a light source allowed then to record the diffraction pattern on the smartphone screen.
The spectra in figure 10 were taken of plasmas both in the new cell and the closed cell. Most noticeably, the plasma in the new cell had a stronger cyan line. To check for the hypotheses of air leak or material sputtering, the measured spectra were compared to atomic emission spectra of argon (Ar), main air components (N_2 and O_2) and to the main material of the cell, borosilicate (Si and B). From these five elementary spectra, three showed a strong cyan line (nitrogen, silicon, boron), while two did not (argon, oxygen). After reexamination of the vacuum setup indeed an error was found, which had caused an air leak, and after fixing that immediately a Doppler valley was measured.

Figure 9: Smartphone spectrometer

The plasma investigation in this instance turned out to be just a curiosity, still it might be interesting to apply for further cell characterization.

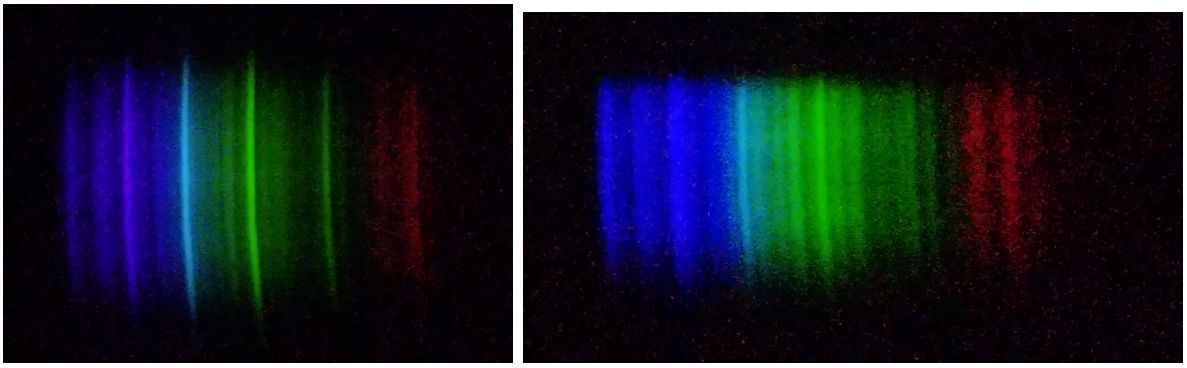

Figure 10: Plasma emission spectra of new cell in vacuum setup (left) and old closed master cell (right). A stronger cyan line can be seen on the left. Both pictures were taken with the authors smartphone camera, with entrance slit and grating as described in section 3.5.

3.6 Cell Production

The vacuum setup was also used to produce closed argon cells, which are used in spectroscopy units in the main experiment to lock lasers. Three cells were produced, one was used to replace an old cell that had stopped working, the other two were kept in spare. The production procedure was the following. The cell was connected to the pumped vacuum section. Then, pressure was set on through-flow. This means the argon bottle was opened and gas could continuously flow into the vacuum, where it was all the time pumped out, creating a pressure equilibrium. When a pressure equilibrium was reached, plasma was ignited with the helical resonator and kept burning for some hours. During this time, the plasma sputtered material of the walls of the inner cell, cleaning it. The argon flow was then stopped, which emptied the cell completely due to the ongoing pumping. This procedure was repeated three to four times. During this, the plasma was monitored with the spectroscopy setup to ensure that a Doppler valley was observed and thus the quality of the plasma was good. Afterwards, the cell let burning for another one to two days. Then a final pressure was set, the glass valve was closed, and the cell was melted off at

a glass blowery facility on the campus.

The final pressure was chosen to be $1 \cdot 10^{-1}$mbar. If there was too much argon in the cell, the spectroscopy beams were absorbed completely and no Lamb-Dip could be measured. If there was too little argon in the cell, plasma ignition became difficult and unstable, making the signal too weak to reliably lock onto.

4 Measurements

In this chapter the measurements carried out in this thesis are described and their results discussed.

4.1 Line broadening

It was investigated to which extend the line broadening effects described in section 2.3 could be measured in the plasma. These measurements were done for different pressures, to test the predictions of pressure broadening.

Measurement procedure Argon gas was put on the through flow mode (see section (3.3) and pressure adjusted to the desired value. Plasma was ignited with the helical resonator with N=12 windings, and the absorption signal recorded with the Doppler free absorption setup. The laser intensity was $I_0 = 430\mu$W. The RF frequency was tuned via the absorption signal until the absorption was maximal. The spectrum was then saved, and the next pressure adjusted. Two measurement runs were done, with pressure ranges of $1.6 \cdot 10^{-2}$mbar to $1.7 \cdot 10^{-1}$mbar in the first run, and $4.0 \cdot 10^{-2}$mbar to $1.8 \cdot 10^{-1}$mbar in the second run.

4.1.1 Doppler broadening

For this analysis, a Gaussian function was fitted to each spectrum. The obtained Doppler widths were then plotted against their respective pressure, see figure 11. The error in the Gaussian width was estimated to be 4% due to pressure inaccuracies. A more detailed discussion of different error sources is given in section 4.3.3.

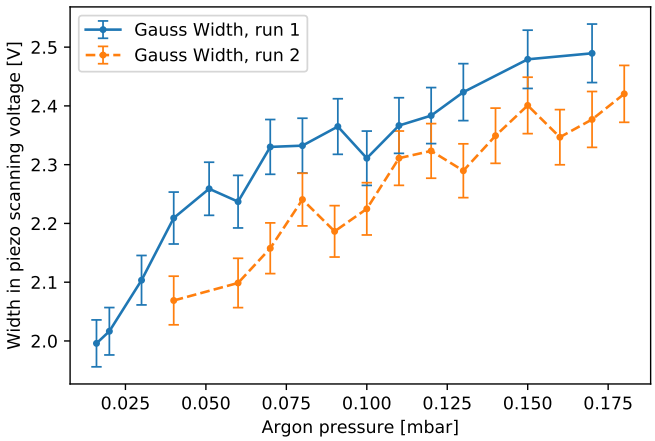

Figure 11: Doppler widths of the absorption spectra for different argon pressures.

It could be observed that the Doppler width increased with pressure. As the plasma temperature is linked with a square-root to the Doppler width, $\Delta\nu \propto T^{1/2}$, (eq. 2.5), we can see that the plasma temperature increased with pressure. The change in plasma temperature between coldest and hottest plasma can be calculated via the largest and smallest Doppler widths, which can be read off of figure 11.

$$\frac{T_{max}}{T_{min}} = \frac{\Delta\nu^2_{max}}{\Delta\nu^2_{min}} = \frac{(2.45)^2}{(2.00)^2} = 50 \pm 4\% \tag{4.1}$$

The plasma temperature increased by 50±4% over the pressure span of one order of magnitude in the first run, and by 37±4% over a pressure span of one half order of magnitude in the second run. Such a temperature increase might be explained by the increased density in the plasma, leading to more charged particles, which then allows the helical resonator to couple more power into the plasma. The increase in atom number can be estimated with the ideal gas law, $n = p/(k_B T)$, which was already used in the theory section, e.g. in 2.8. With increased temperature by a factor of 1.5 and increased pressure by a factor of 10, this leads to an estimated increase in density by a factor of 6 to 7. Such an increased amount of charged particles could explain how the resonator can couple more power into the plasma.

4.1.2 Pressure broadening

For this analysis, a Gaussian was fitted to each spectrum. The Gaussian was then subtracted from the data, and a Lorentzian was fitted onto the remaining data, i.e. the Lamb-Dip. The Lorentzian fitting procedure was much less precise than the Gaussian one, because moderate changes in the fitting changed the Lorentzians by up to 10%. One had to iteratively narrow down the fitting parameters until a decent fit was reached. Thus an error of 10% is estimated for both Lamb-Dip width and Lamb-Dip height, superseding all other experimental error sources. They are plotted on the left and right in figure 12.

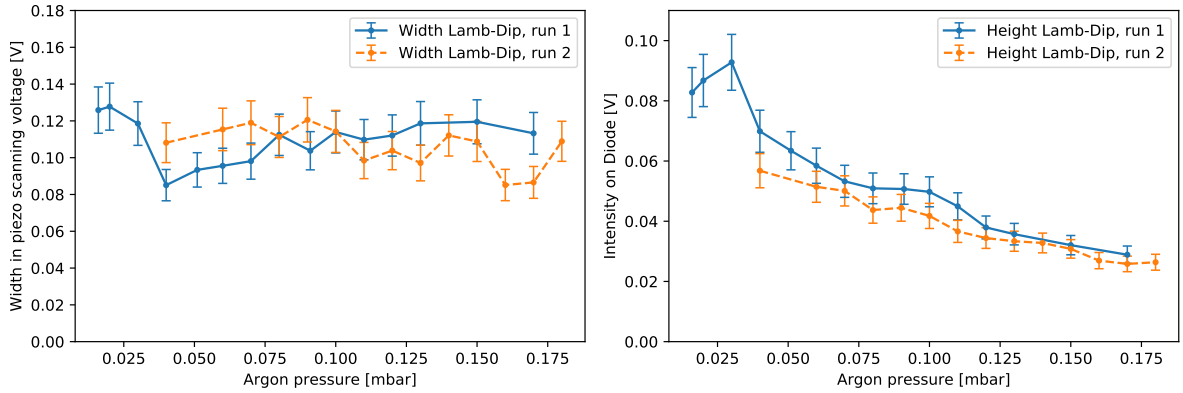

Figure 12: Measured Lamb-Dip Width and Height

The Lamb-Dip width fluctuates a little bit, but within the error bounds it stays constant. If the Lamb-Dip width would just stem from the natural line width, this data would exactly match expectation, as the natural line width is constant. However, we estimated in section 2.3.3 that the effect of resonance broadening should be at least on the order of the natural line width, and this estimation was even done for the lower pressure end (0.03mbar). Resonance broadening is predicted to scale linearly with density (eq. 2.6), so at least for the high pressure end, we would have expected an observable increase in Lamb-Dip width. To give two example values, for a pressure of 0.03mbar the predicted pressure broadening was 23 MHz, and for a pressure of 0.3mbar (tenfold increase), if one takes the estimation done in the previous section 4.1.1 that the density thereby increased by a factor 6-7, this would lead to a predicted broadening of 138-161 MHz. This would be a massive broadening but since we don't see it, it might be that our theory is not accurate, and the employed formula for resonance broadening does not apply to our experimental conditions.

On the other hand, the Lamb-Dip height shows a clear trend. The height decreases with increasing pressure. This can be explained by the pump-probe interaction described in 2.4. As the pressure increases, more atoms remain in the lower level, as the pump beam only excites a fixed amount of atoms (as its power stays constant). The probe beam is then more absorbed by the increased amount of lower level atoms, which reduces its intensity, and thus the height of the Lamb-Dip.

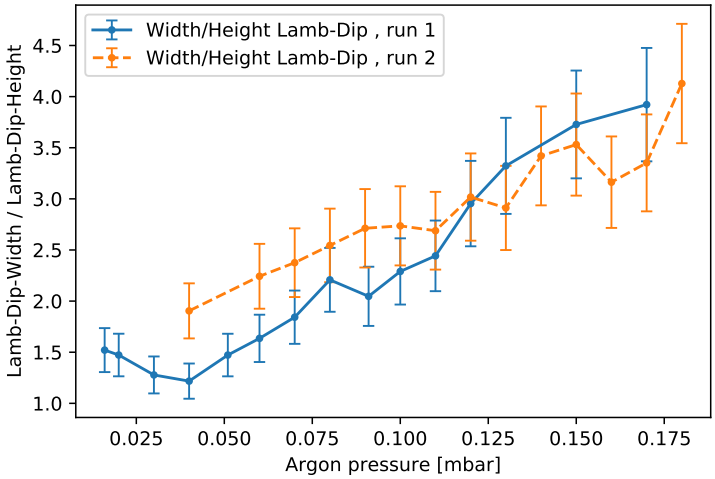

Figure 13: Ratio of Lamb-Dip width to height.

If one looks at the ratio of the Lamb-Dip widths to heights, an increase of this ratio with pressure of this ratio can be seen, shown in figure 13. However, we can't really interpret this as pressure broadening, as our theory and understanding is that pressure broadening would manifest mainly in the Lamb-Dip width, while the Lamb-Dip height is a separate technical effect due to the spectroscopy setup.

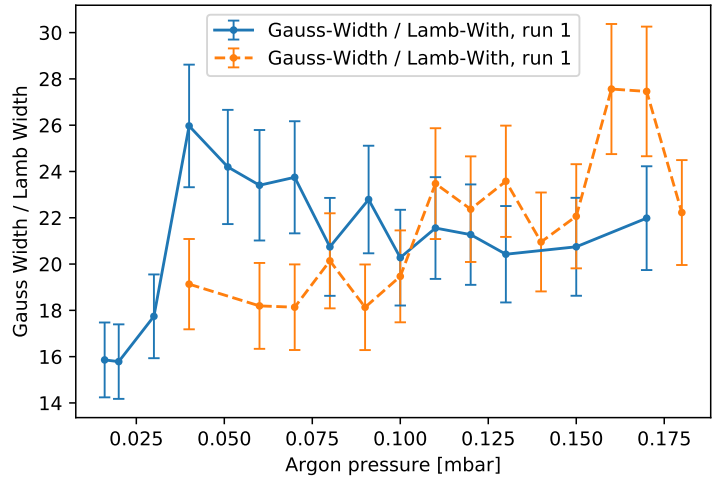

Figure 14: Measured ratio between Doppler width and Lamb-Dip width. Theory predicted a ratio of about 30.

To investigate one further prediction of theory, the ratio between Gaussian width and Lamb-Dip width was looked at. Measurements are plotted in figure 14, showing a ratio of 23±5 constant over pressure, while theory predicted a ratio of 30 or higher (because Doppler width was calculated as a lower bound), as was listed in table 1.

$$Theory: \quad \frac{\Delta\nu_{Gauss}}{\Delta\nu_{LambDip}} = 30 \tag{4.2}$$

$$Experiment: \quad \frac{\Delta\nu_{Gauss}}{\Delta\nu_{LambDip}} = 23 \pm 5 \tag{4.3}$$

Theory and measurement are, within a 2σ-error in agreement with each other. However, our measured ratio is lower than the predicted one, which is striking because this means that we observe a stronger Lamb-Dip broadening than predicted, while simultaneously we measured no pressure broadening on the Lamb-Dip over a one order of magnitude in pressure. If the Lamb-Dip was only given by the natural line width Γ, we would measure a ratio of $\Delta\nu_{Gauss}/\Gamma = 730$ MHz / 9.28 MHz = 79, at least, because of the lower bound on the Doppler width. Compared to the Lamb-Dip width, this gives a ratio of at least $\Delta\nu_{LambDip}/\Gamma = 79/23 = 3.4$, which means that the Lamb-Dip is at least 3.4 times larger than the natural line width, at $\Delta\nu_{LambDip} = 3.4\ \Gamma = 31.5$ MHz.

As this observed Lamb-Dip width stayed constant over one order of magnitude of pressure changes, we suspect that it might not be caused by pressure broadening, but by other effects. One possibility that was not considered until now was power broadening, where too high laser intensity leads to a broadened absorption. For the employed quench transition $1s_5$-$2p_8$, the saturation intensity is $I_s = \pi hcA_{21}/(3{\lambda_0}^3) = 370\mu\mathrm{W/cm^2}$ [5], while our laser intensity was at $I_0 = 430\mu$W at a beam diameter of ca. 3mm, leading to a power broadened linewidth of $\Gamma' = \sqrt{1 + I_0/I_s}\ \Gamma = \sqrt{1 + 16.4}\ \Gamma = 4.1\ \Gamma$. As the broadening was measured to be of factor 3.4 or higher and the estimated power broadening is of factor 4.1, power broadening seems a promising explanation for the observed data, although it was not considered in the beginning.

4.2 Gas mixing

Helium and air were added into the argon plasma cell in controlled amounts. The resulting new metastable densities were measured and are shown in figure 15. In literature, most mixing experiments reported decreased metastables, but [10] and [11] showed positive results in their setups.

The argon gas was put on continuous through-flow, and argon pressure was set to $2.85 \cdot 10^{-2}$mbar. Then, controlled amounts of Helium or Air were let into the cell additionally, increasing the total pressure in the cell. Plasma was ignited with the helical resonator with N=12 windings, and the absorption signal was recorded at laser intensity $I_0 = 1.2$mW. The RF frequency was tuned until absorption was maximal, then a spectrum was saved.
For Air, an immediate and drastic absorption decrease was observed already at the first mixing pressure. At the next pressure the absorption signal almost disappeared, which is why the measurement was already terminated after two measurements. For Helium, mixing ratios p_{He}/p_{Ar} between 0.1 and 2.5 were tried. The metastable densities were calculated via the procedure described in section Data Analysis (4.3.2) in more detail, and are shown in figure 15. As can be seen, both Helium and Air reduced the metastable density in the plasma significantly. This result was the expected outcome, as most experiments in literature reported such decreased densities for mixing. However, further experiments could be tried with e.g. Xenon or Krypton, for which ref. [11] still reported positive results in an experimental setup quite similar to this one.

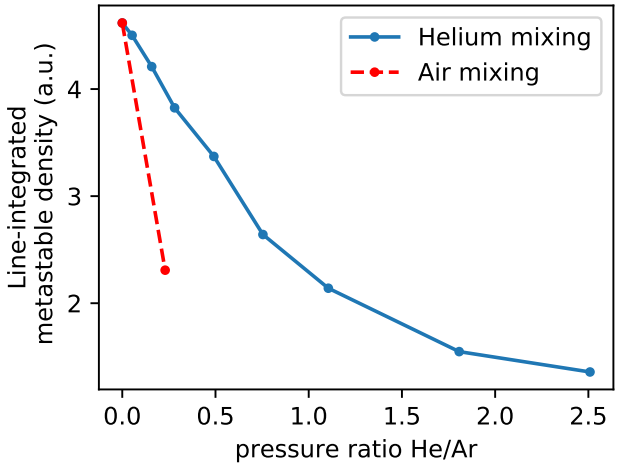

Figure 15: Mixing of helium and air into the argon plasma. The x-axis shows the ratio of relative pressures, p_{He}/p_{Ar} or p_{Air}/p_{Ar} for helium or air, respectively. The partial pressure p_{Ar} of argon has been kept constant at $2.85 \cdot 10^{-2}$mbar, the partial pressures of helium and air were changed. Errors were negligibly small (<2%) and would not be seen in the plot.

4.3 Helical Resonator optimization

The helical resonator is a central component in metastable production, as it provides the electric field that drives the plasma. In the current ArTTA setup, the efficiency of metastable production is ca. 10^{-4}, that is, one in a thousand argon atoms ends up in the metastable state. There is ongoing research to increase this efficiency. One part is in optimization of the Helical Resonator, for example in it's geometry, materials, input signal and positioning.
In this thesis, optimization experiments were conducted on the Source Helical Resonator (N=5), in which its geometry and operation were modified and the resulting metastable densities recorded. The optimization setup is now explained, followed by the obtained data and interpretation.

4.3.1 Free parameters

For optimization, the following free parameters were investigated. In most runs, one parameter was varied, and the other ones were kept constant.

- **Tapping wire position.** It is known from theory that changing the position where the tapping wire connects to the antenna influences the impedance of the resonator, and thus its possible power input. To investigate this, 19 positions along the antenna were chosen, on which the tapping wire was soldered onto. These positions where spaced at steps of approximately 45°to each other to give a reasonable resolution along the antenna. The positions can be seen sketched in figure 16.

- **Tapping wire length.** Two lengths of tapping wire were employed, 7cm and 3cm. The 3cm wire was employed in a comparison measurement, labelled as such. All other measurements were done with the 7cm wire.

- **Matching Box.** An impedance matching box could be inserted between amplifier and resonator. This was done in a comparison measurement, labelled as such. All other measurements were done without matching box, where amplifier and resonator were directly connected with each other through a 30cm BNC-Cable.

- **Resonator placement** The positioning of the resonator along the glass cell was conducted for three discrete placements, called Front, Mid, and Back. The Front placement is shown in figure 17, where the resonator aligns on the right with the end of the cell. Mid was the case in which the resonator was in the center of the cell, and Back when it touched the glass rod on the other end of the cell.
- **RF frequency.** The RF frequency could be varied in the range of 130-220 MHz.

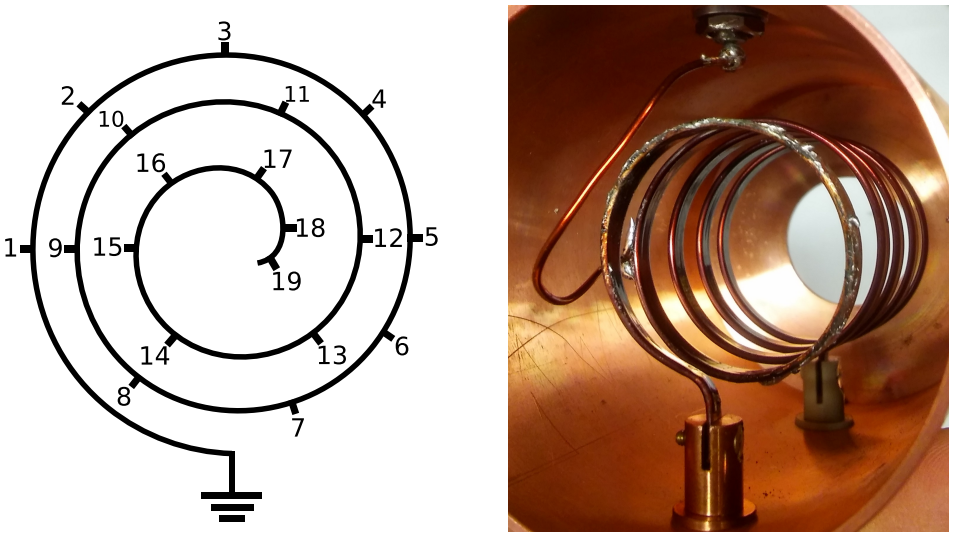

Figure 16: Left: Tapping wire positions, labelled 1-19 along the antenna. Right: A picture of the helical resonators inside, were the tapping wire is connected on the antenna, on tapping position 9. The helical resonator has an open and a shielded end, the picture is taken through the open end, and the shielded end can be seen in the back. The hole in the shielded end has the purpose to let the glass cell pass through.

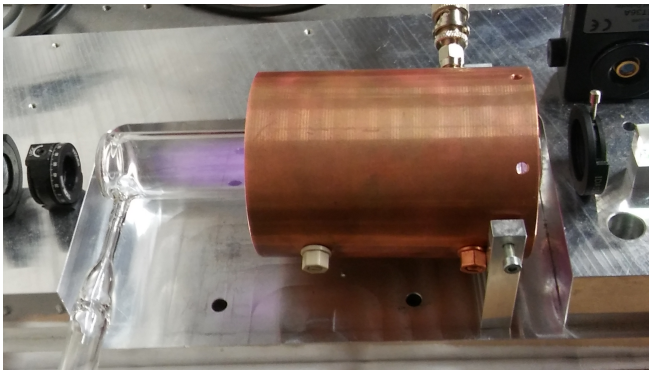

Figure 17: Glass cell surrounded by the resonator. Laser optics can be seen on the sides. The resonator is in the Front placement.

4.3.2 Measurement procedure and Data Analysis

Here the measurement procedure and data analysis are given. Actions are listed in chronological order.

Measurement procedure

1. The pressure in the cell was set to $2.85\,(\pm 0.05) \cdot 10^{-2}$mbar in the through flow mode (see section 3.3). This pressure was monitored continuously and readjusted in case. The laser intensity was 1.2mW.

2. The tapping wire length was chosen and soldered onto the BNC-Plug of the Resonator.

3. The tapping wire position was chosen, and the tapping wire soldered to this position on the antenna.

4. The resonator was placed around the glass cell and the laser spectroscopy block was aligned until intensity of the laser light going through the empty glass cell was 1.8 ± 0.1V on the diode, and the absorption profile was as flat as possible with less than 0.05V intensity deviation over all frequencies scanned by the laser. Details of this alignment are addressed in section 3.4.

5. The resonator placement was chosen.

6. The amplifier was turned on and the plasma was ignited. This procedure took 5-60 seconds, depending on the tapping wire position, and some different RF frequencies had to be tried.

7. The RF frequency was tuned until a local absorption maxima was observed. The broad tuning could be performed by looking at the plasma brightness, the fine tuning was done via the absorption signal. The plasma brightness and absorption signal were highly correlated. When an impedance matching box was used, impedances and RF frequency were walked together until an absorption maximum was observed.

8. The absorption spectrum was measured and saved, along with the current RF frequency.

9. Procedure was now repeated for other choices in these steps.
   - Back to 7: Another RF frequency was searched where the absorption had a local maximum.
   - Back to 5: Another resonator placement was set.
   - Back to 3: Another tapping wire position was soldered.

Data Analysis

In figure 3, a typical absorption spectrum is shown. For such a spectrum, data analysis was carried out in the following way. The incident intensity I_0 was reconstructed through the intensities at the left and right border of the absorption spectrum. The intensities didn't change whether plasma was burning or not, preserving the initial intensity. Specifically, the first and last data point of the measured intensity array $I[i]$ (corresponding to the lowest and highest scanned laser frequency) were chosen to reconstruct I_0.

$$I_0 = \frac{I[0] + I[len-1]}{2} \tag{4.4}$$

The line-integrated metastable density was then calculated through the formula introduced in eq. 2.11, and the constants have been left out, as they were not relevant for relative measurement.

$$\langle n_{1s5} \rangle L = \int_{[Data\,points\ i]} ln\left(\frac{I_0}{I[i]}\right) \tag{4.5}$$

The absorption profile width $\Delta\nu$ (see eq. 2.11) did not change considerably throughout all measurements, it was omitted for faster data analysis. As absorption depth $ln(I_0/I)$ and absorption width $\Delta\nu$ were positively correlated with each other, taking into account also the absorption width would have resulted in the same plots qualitatively, but a little bit more stretched relative differences in the y-direction.

An exemplary plot is shown in figure 18 and some details are given there on how the plots in the following sections can be read.

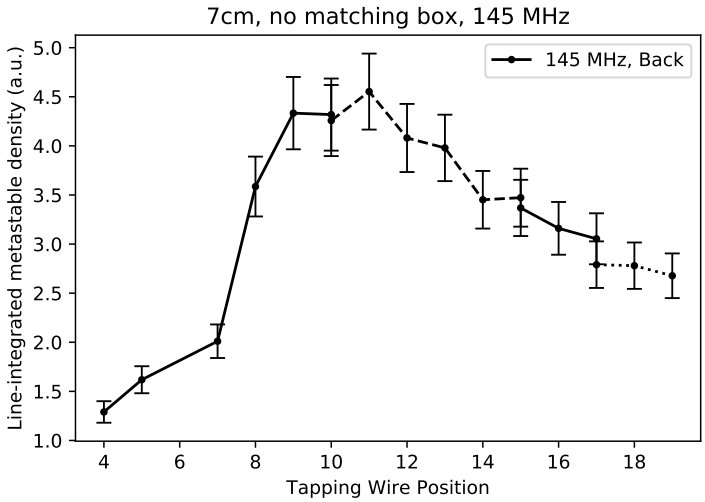

Figure 18: Plot: Along the x-axis the soldered tapping wire positions are given for which the metastable density was each measured. The metastable density is given in arbitrary units (a.u.) as we are interested only in relative comparisons. The additional parameters that have been kept constant during the measurement are given in the title. The tapping wire length was 7cm, no matching box was used, and the 145 MHz means that this plot only shows metastable maxima that where found with RF frequencies of 145±5 MHz. The plotted line is given for the resonator in the Back placement. The three different dashed lines represent that the data has been taken on three different days. Small jumps in between those measurements can be seen, e.g. at tapping wire positions 17, because no interpolation was done between different days to preserve the original data. In the following plots the differentiation by day is omitted to focus on other parameters. An error of 8.5% is attached to each data point corresponding to the error estimation in section 4.3.3.

4.3.3 Errors

An overview of different error sources and an estimate of their influence on the metastable density are given in the following.

- Argon pressure. 3-4%. The pressure could be controlled up to fluctuations of $0.1 \cdot 10^{-2}$mbar which occurred on the order of seconds. These fluctuations led to the total pressure varying between $2.80 - 2.95 \cdot 10^{-2}$mbar.

- Glass cell transmission. 3-6%. Even if the plasma stayed the same, a small change of the laser angle relative to the glass cell led to different transmitted intensities, resulting in a different calculated metastable density. To cope with this it was crucial to have unchanged transmission intensities over all measurements which was possible up intensity variations of 0.1 V. Comparison measurements showed that changes of 0.2 V in the intensity lead to changes in the calculated metastable density between 3-6%.

- Frequency tuning. 1%. Frequencies were tuned with live feedback of the absorption depth, and could be tuned until the absorption was maximal. The resonance frequencies could be determined up to ±3 MHz, as the maxima then did no longer change noticeably.

- Resonator placement. 2-3%. The resonator placement was adjusted by eye, with a precision of ca. half a cm. Moving it within this margin led to metastable changes of 2-3%. The Mid placement was defined by a painted marker, Front and Back by the borders of the cell.

- Soldering. 1-3%. The tapping wire positions were soldered with an accuracy of ca. 10°. As the different positions were spaced by approx. 50°, this corresponds to a relative accuracy of 20% to the next position. Such a difference in tapping position lead to metastable density changes of 1-3%.

Adding the single errors together quadratically, and taking the upper limits for each single error source, a combined error bound of 8.5% on the metastable density was obtained.

4.3.4 Resonance frequencies

Through all scanned RF frequencies, those that gave rise to a local absorption maximum are shown in figure 19, which is now discussed. Two distinct frequencies can be seen, 145(±5) MHz and 195(±5) MHz, that led to maximal absorption over all tapping wire positions and all resonator placements. Thus we call these two frequencies resonance frequencies, or modes. The first mode at 145 MHz was expected from theory (table 2), but the second mode at 195 MHz was not. A third intermediate mode was observed around 170 MHz, which however could not be ignited as reliably as the other two, and fluctuated more with different resonator and tapping wire position. We will restrict thus the following discussions to the two more stable modes, 145 MHz and 195 MHz.
The 145 MHz mode was predicted by equation 2.12, and it further fulfills the quarter-wave condition: $\lambda/4 = 51.7$cm matching almost exactly the antenna length $l = 53$cm. For the 195 MHz mode on the other hand, no such geometrical correspondence could be found. It has a quarter-wavelength of $\lambda/4 = 38.4$cm. When searching for other explanations, two effects were found that could contribute. First, antennas can be operated at additional modes, for example in $3/4\lambda$-wave or $5/8\lambda$-wave operation. The 5/8-wave is reported to provide a power gain over the quarter wave, and an increased amount of power radiated at lower angles (16°compared to 20°for 1/4 operation) [24] [25]. For 195 MHz ($\lambda_0 = 153.7$) this would calculate to $(1/2)5/8\lambda_0 = 48.0$cm. The factor of one half stems from the fact that the helical resonator is already a device designed halve normal dipole antennas ($\lambda/2$) to quarter wave antennas ($\lambda/4$) in order to reduce the needed antenna length in half, which save much material at meter-long wavelengths. The second contributing effect could be that signals propagating inside an insulated cable have shortened wavelengths λ_e

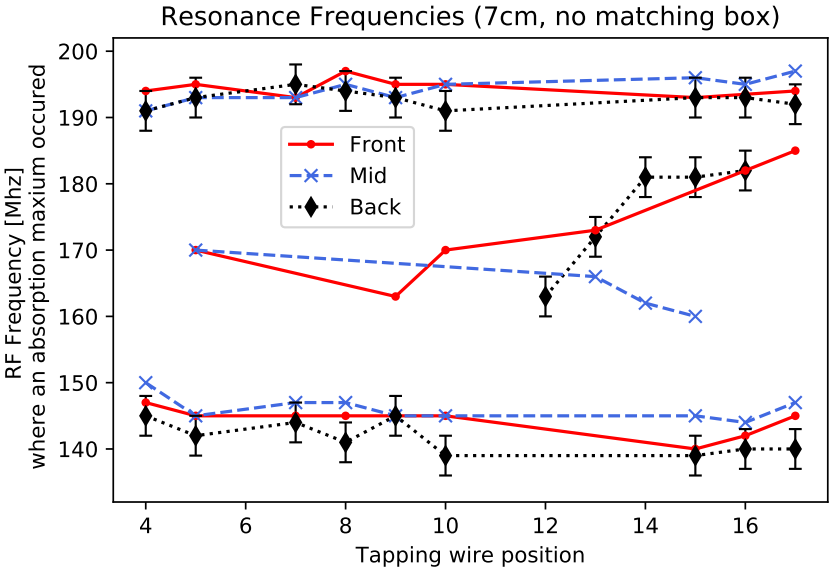

Figure 19: Overview on the RF frequencies where an absorption maximum occurred in the plasma. Two distinct modes can be seen, 145 MHz and 195 MHz, that are invariant to tapping wire position. A less reliable behaviour can be seen for a third mode in the center at ca. 170 MHz. The error of ±3 MHz applies to all values but is plotted for better readability only for the Back placement.

compared to their wavelength in vacuum, λ_0. This is due to interactions with the dielectric insulation material of cables. The effective wavelength can be calculated via $\lambda_e = \kappa\lambda_0$, where $\kappa < 1$ is a material specific constante called velocity factor, with a typical value of $\kappa_0 = 0.659$ [26]. For 195 MHz, this would calculate to $(1/2)\lambda_0\kappa_0 = 53.4$cm. Interestingly close.

Length of BNC cable In a single measurement, the length of the BNC cable between amplifier and resonator has been changed from 30cm to 200cm. This shifted the resonator modes higher by 10-15 MHz, which is a sign that the BNC cable is also part of the resonator system and might influence the plasma. Further investigations on the lenght of the BNC cable are better suited for the final ArTTA experiment as the BNC cable can there still be changed easily at any time.

4.3.5 Tapping wire position & Resonator placement

The higher the metastable density, the better. For better comparison, the y-scalings are equal for each pair of plots. To begin our discussion, we look at the influence of the tapping wire position onto the metastable density, shown in figure 20. The 145 MHz mode has a central maximum at tapping wire positions 10-12, while the 195 MHz mode does not show such a maximum, but increases steadily and reaches a plateau. Both modes reach equal maxima.

In figure 20 also the performance of the resonator placements is shown, which is now discussed. For the 145 MHz mode, all three placements show similar behaviour, within errors they are the same. At 195 MHz instead, the placements behave differently. Front and Back continue to rise, while the Mid placement gets considerably worse for high tapping wire positions. This could be an indication that the 195 MHz mode couples more

energy in spaces outside of the antenna than the 145 MHz mode, which would fit with the characteristics of $5/8\lambda$-wave operation described in section 4.3.4. In figure 20 two lines for each resonator placement can be seen for the 195 MHz mode, this is because this section was measured twice and both measurement runs a plotted together.

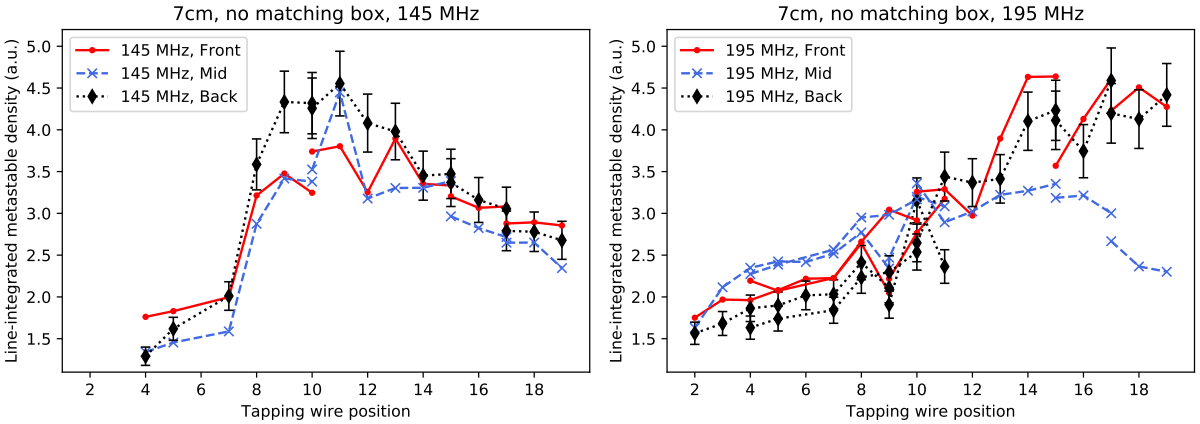

Figure 20: Performance of the tapping wire positions and the three resonator placements Front, Mid, and Back. The error is 8.5% on all points, but for better readability only plotted on the Back placement.

4.3.6 Tapping wire length

The performance of the two tapping wire lengths 7cm and 3cm is shown in figure 21. At 145 MHz, both wire lengths show very similar behaviour. The 3cm wire shows slightly better results, but within errors no difference can be seen. At 195 MHz, the is a small distinction. Placements Back and Mid behave the same for both wire lengths, and again it can be seen that the Mid placement decreases for high tapping positions. However, the Front placement for the 3cm wire shows an exceptionally good result at 195 MHz, the highest recorded metastable density within the whole explored parameter regime. It has a 20% higher metastable density than the best result for the 7cm wire. We also see here again the characteristic that Front and Back placements perform better than the Mid placement. It is interesting that Front performs better than Back, because in the Front placement some of the plasma is separated from the antenna through a shielded end of the resonator, which can be seen in figure 16 in the background.

4.3.7 Impedance matching

Lastly, we take a look at the performance of the impedance matching box, shown in figure 22. The impedance matching box was tuned to maximal absorption signal, thus maximal metastable density. When it was not used, amplifier and resonator were just linked directly with a BNC-Cable. For both modes 145 MHz and 195 MHz, the results with matching box were worse than without, metastable density decreased by up to a factor of 2. This is striking, because the matching box was thought to increase power delivery to the plasma as described in section 2.6.2, especially if it was explicitly tuned onto maximal absorption as done here. One explanation might be a technical defect in the box, that introduces additional unwanted resistances. As there exists a second matching box in the ArTTA experiment, of same manufacturer and type, this could be used in a future comparison, to check for potential technical defects. Another explanation could be

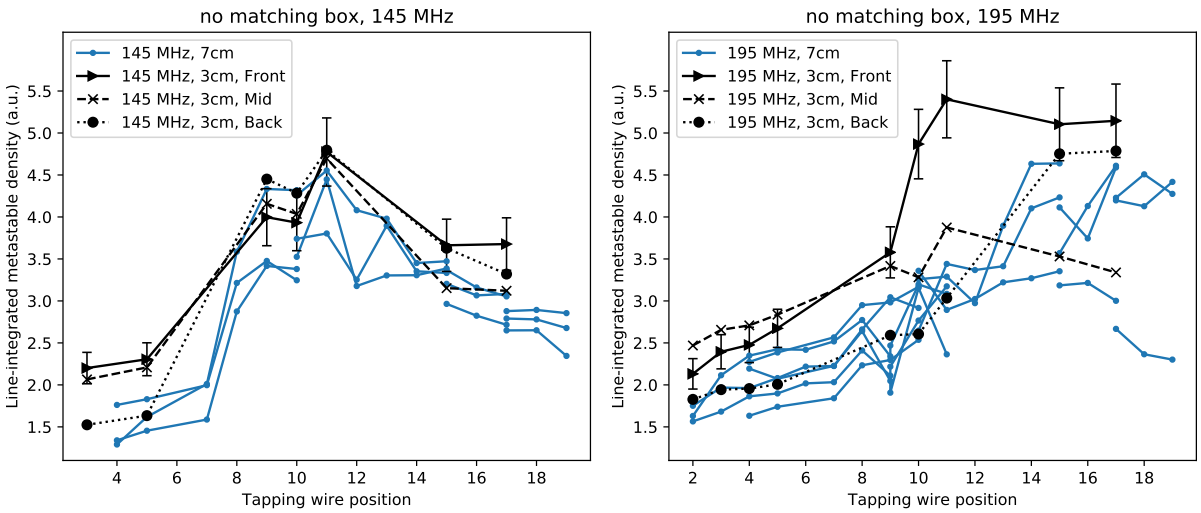

Figure 21: Performance of the tapping wire lengths 7cm and 3cm. The error is 8.5% for all data points, but for better readability only plotted on the best performing curve.

that the two 1m-long cables connecting from matching box to amplifier and resonator were already long enough to damp the signal.
A second observation concerning the matching box it's results (black lines, dashed) look very similar both modes 145 MHz and 195 MHz, while the non-matched curves (blue lines, solid) are very different compared between 145 MHz and 195 MHz. This could indicate that with the matching box for each tapping wire position some maximal absorption was possible, and this maximum could be reached through correct tuning regardless of the given frequency .

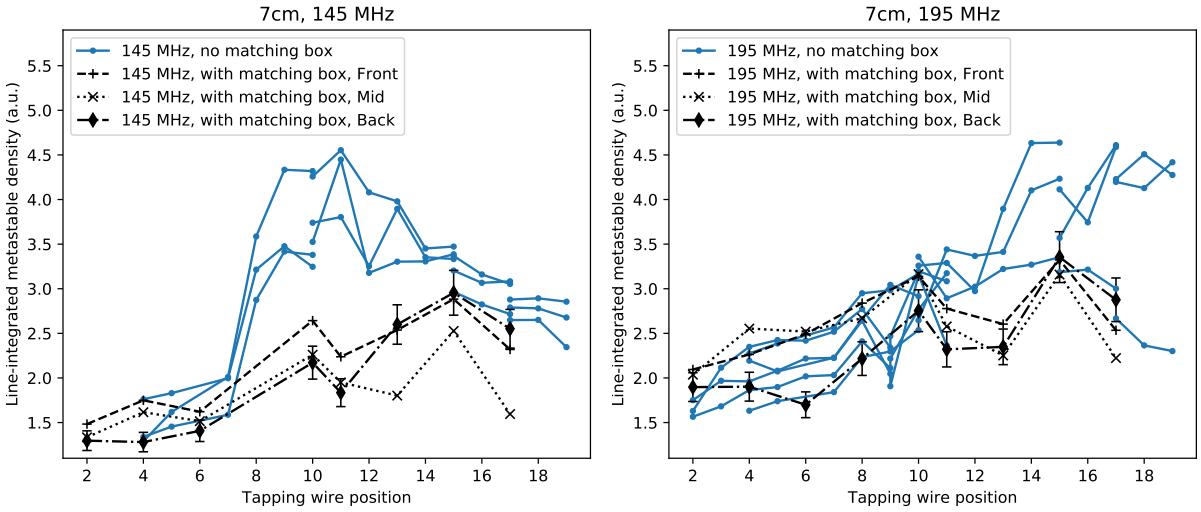

Figure 22: Performance of the impedance matching box. The error is 8.5% for all points, but for better readability only plotted on one curve.

5 Conclusion

Line broadening of the Lamb-Dip
A broadening effect of ca. 3.4 times the natural line width could be observed. This broadening however could not be explained via the anticipated pressure broadening as it stayed constant over all tested pressures. Instead it could be best explained by power broadening, an effect that was not considered in the beginning. The theory for pressure broadening predicted widths up to 138 MHz which are suspiciously large. This indicates that the theory was not suited well for our plasma regime, and we may have overlooked some additional constraints.

Gas mixing
Helium and air mixing showed a clearly reduced metastable density, therefore quenching the metastable production.

Smartphone spectroscopy
The DIY smartphone spectrometer allowed to take emission spectra of the cells. The spectral lines could be qualitatively compared to known atomic spectra, giving hints on the atomic species in the plasma.

Helical resonator optimization

- A second unexpected mode at 195 MHz appeared, that performed up to 15% better in metastable production than the 145 MHz mode. Both Modes showed qualitatively different dependencies on the tapping wire position. A reason for the second mode could be $5/8\lambda$-wave antenna operation or dielectric insulation effects.
- The tapping wire position influenced metastable densities by up to a factor of 4. The positions 1-7 performed worst while the positions 8-17 performed better, achieving higher metastable densities.
- The 3cm tapping wire performed up to 20% better in metastable production than the 7cm wire.
- The plasma was best burning if the resonator was moved on either side of the glass cell such that the plasma was located mostly outside of the antenna. This effect was observed for the 195 MHz mode, while the 145 MHz mode showed no distinction between placements.
- The matching box surprisingly made results worse, up to a factor of 2. From theory it was thought that it could only improve the results.

The singular best configuration found for metastable production was: tapping wire length 3cm, tapping wire connected to tapping position 11, RF frequency 195 MHz and no matching box.

Outlook
It would have been great to have the measured broadening widths in MHz, and not just in Piezo scanning voltages. This could be measured in future with a Fabry-Pérot-Interferometer, and then Piezo voltages given in this thesis could be converted to MHz for more insight. The matching box could be compared with a second matching box available at the ArTTA experiment, to rule out a simple technical defect.

Lastly, the position of the plasma relative to the resonator influenced the metastable density by a factor of up to 2. Studying this spatial dependency in more detail would be great, especially since it only occurred for the 195 MHz mode, indicating different power radiation patterns.

Acknowledgements

Ich möchte mich als Erstes bei Prof. Dr. Markus Oberthaler bedanken. Dafür dass ich meine Bachelorarbeit in seiner Arbeitsgruppe schreiben konnte, und dass er immer ein offenes Ohr für Fragen hatte, und uns immer tatkräftig unterstützt hat. Prof. Dr. Werner Aeschbach danke ich dass er die Zweitkorrektur übernommen hat.
Meine Zeit am Experiment wäre nicht denkbar gewesen ohne dem ATTA-Team Lisa Ringena, Julian Robertz und Maximilian Schmidt. Sie haben sich die Zeit genommen mir von Beginn an alles zu erklären und standen mir im Labor täglich zur Seite. Das war echt toll, vielen Dank Lisa, Julian und Max. Der gesamten SynQs/Matterwave Gruppe muss ich danken für die tolle Atmosphäre, zum beispiel dem Freitagsfrühstück, einer sehr schönen Tradition.
Für das Korrekturlesen muss ich mich besonders bei Lisa bedanken. Sie hat ausführlich und mehrere Male meine Entwürfe gesichtet und ihnen die nötige Struktur gegeben, ohne sie wäre diese Arbeit so nicht zustandegekommen. Weiterhin bedanke ich mich bei JP, Maxa, Sophie und Anja für die vielen kleinen gefundenen Satzzeichen und Wörter die so noch nicht ganz richtig untergebracht waren: Where were you. Abschließend möchte ich meinen Eltern danken. Sie haben das alles überhaupt erst möglich gemacht und standen mir immer zur Seite.

References

[1] H.H.Loosli et al., “Ten years low-level counting in the underground laboratory in Bern, Switzerland”. In: *Nuclear Instruments and Methods in Physics Research B17 (1986) 402-405* ().

[2] W. Kutschera et al., “Long-lived noble gas radionuclides”. In: *Nuclear Instru- ments and Methods in Physics Research Section B: Beam Interactions with Materials and Atoms, 92(1-4):241 – 248* (1994).

[3] Z.-T. Lu. et al. C. Y. Chen, “Ultrasensitive Isotope Trace Analyses with a Magneto-Optical Trap”. In: *Science, 286(5442):1139– 1141* (1999).

[4] Joachim Welte, “Atom Trap Trace Analysis of 39Ar”. PhD thesis. Heidelberg, 2011.

[5] Florian Ritterbusch, “Dating of groundwater with Atom Trap Trace Analysis of 39Ar”. PhD thesis. Heidelberg, 2013.

[6] Sven C. Ebser, “Dating of Ice and Ocean Samples with Atom Trap Trace Analysis of 39Ar”. PhD thesis. Heidelberg, 2016.

[7] Zhongyi Feng, “Quantum technological dating of glacier ice from the last millennium and a new self-contained facility for routine measurements”. PhD thesis. Heidelberg, 2018.

[8] Markus Kohler, “Vakuum-Ultra-Violette-Lichtquelle und Konzeption für die Ultraspurenanalyse von seltenen Kryptonisotopen”. PhD thesis. Hamburg, 2011.

[9] Sergey G. Belostotskiy et al., “Spatially Resolved Measurements of Argon Metastable (1s5) Density in a High Pressure Microdischarge Using Diode Laser Absorption Spectroscopy”. In: *IEEE Transactions on Plasma Science, Vol. 37 No. 6* (2009).

[10] Alan R. Hoskinson et al., “Argon metastable production in argon-helium microplasmas”. In: *Journal of Applied Physics119, 233301 (2016); doi: 10.1063/1.4954077* (2016).

[11] P. Mueller K. Rudinger Z-T. Lu, “The role of carrier gases in the production of metastable argon atomsin a rf discharge”. In: *Review of Scientific Instruments 80, 036105* (2009).

[12] G. A. Hebner and P. A. Miller, “Behavior of excited argon atoms in inductively driven plasmas”. In: *Journal of Applied Physics; PBD: 7 Dec 1999* ().

[13] Shahid Rauf and Mark J. Kushner, “Argon metastable densities in radio frequency Ar, Ar/O2and Ar/CF4 electrical discharges”. In: *J. Appl. Phys.82(6), 15 September 1997* ().

[14] Jared A. Miles, “Determining Metastable Densities in an Argon Discharge Through Optical Emission Spectroscopy”. MA thesis. Wright State University, 2010.

[15] Gornushkin et al., “Line broadening mechanisms in the low pressure laser-induced plasma”. In: *Spectrochimica Acta Part B 54 1999 1207-1217* (1999).

[16] G. Peach, “Theory of the pressure broadeningand shift of spectral lines”. In: *Advances in Physics, 30:3, 367-474* (1981).

[17] C.S. Lee et al., “Van Der Waals Broadening Absorption Lines”. In: *J. Quont. Speclrosc. Radial. Transfer. Vol. 15, pp. 211-216. Pergamon Press* (1975).

[18] K. Katsonis et al., "Argon 4s and 4p Excited States Atomic Data Applied in ARC-JETModeling". In: *International Journal of Aerospace Engineering Volume 2011, Article ID 896836* (2011).

[19] Wolfgang Demtröder, *Laserspektroskopie: Grundlagen und Techniken*. Springer-Verlag Berlin Heidelberg, 2007.

[20] Marcel Fiebrandt et al., "Measurement of Ar resonance and metastable level number densities in argon containing plasmas". In: *J. Phys. D: Appl. Phys. 50 355202* (2017).

[21] Timo Gierlich, "Design of a fiber-coupled argon laser spectroscopy and investigation of the metastable density in an RF source". MA thesis. Heidelberg, 2017.

[22] Schildknecht R. Macalpine W., "Coaxial Resonators with Helical Inner Conductor". In: *Proceedings of the IRE, 47(12), 2099–2105. doi:10.1109/jrproc.1959.287128* (1959).

[23] Jeffrey Warren, *Build a papercraft spectrometer for your phone – version 2.0*. 2017. URL: https://publiclab.org/notes/warren/11-30-2017/build-a-papercraft-spectrometer-for-your-phone-version-2-0.

[24] Bob Cocco Edward Oros, *The Antenna Elmer - Design Your Own 5/8 Wave Vertical Antenna*. 1997. URL: https://www.qsl.net/w4sat/five8th.htm.

[25] Ian Poole, *Five Eighths Wavelength Vertical Antenna, Electronics Notes*. URL: https://www.electronics-notes.com/articles/antennas-propagation/vertical-antennas/five-eighths-wavelength-vertical.php.

[26] Ian Poole, *Coax Cable Velocity Factor, Electronics Notes*. URL: https://www.electronics-notes.com/articles/antennas-propagation/rf-feeders-transmission-lines/coaxial-cable-velocity-factor.php.

Eidesstattliche Erklärung

Ich versichere, dass ich diese Arbeit selbstständig verfasst und keine anderen als die angegebenen Quellen und Hilfsmittel benutzt habe.

$Unterschrift:$ $Ort, Datum:$